Determination of optimal parameters for dual-layer cathode of polymer electrolyte fuel cell using computational intelligence-aided design

Chen, Yi; Huang, Weina; Peng, Bei

Published in:
PLoS ONE

DOI:
10.1371/journal.pone.0114223

Publication date:
2014

Document Version
Publisher's PDF, also known as Version of record

PLOS ONE

RESEARCH ARTICLE

Determination of Optimal Parameters for Dual-Layer Cathode of Polymer Electrolyte Fuel Cell Using Computational Intelligence-Aided Design

Yi Chen[1,2,3], **Weina Huang**[1,2], **Bei Peng**[1,2]*

1. School of Mechatronics Engineering, University of Electronic Science and Technology of China, Chengdu, 611731, China, **2.** Robotic Research Center, University of Electronic Science and Technology of China, Chengdu, 611731, China, **3.** School of Engineering and Built Environment, Glasgow Caledonian University, Glasgow, G4 0BA, United Kingdom

*beipeng@uestc.edu.cn

Citation: Chen Y, Huang W, Peng B (2014) Determination of Optimal Parameters for Dual-Layer Cathode of Polymer Electrolyte Fuel Cell Using Computational Intelligence-Aided Design. PLoS ONE 9(12): e114223. doi:10.1371/journal.pone.0114223

Editor: Xiao-Dong Wang, North China Electric Power University, China

Received: August 8, 2014

Accepted: November 4, 2014

Published: December 9, 2014

Data Availability: The authors confirm that all data underlying the findings are fully available without restriction. All relevant data are within the paper.

Funding: This work was supported by the National Natural Science Foundation of China (No. 91123023 and 51105061) and the National Program for Support of Top-Notch Young Professionals. The funders had no role in study design, data collection and analysis, decision to publish, or preparation of the manuscript.

Competing Interests: The authors have declared that no competing interests exist.

Abstract

Because of the demands for sustainable and renewable energy, fuel cells have become increasingly popular, particularly the polymer electrolyte fuel cell (PEFC). Among the various components, the cathode plays a key role in the operation of a PEFC. In this study, a quantitative dual-layer cathode model was proposed for determining the optimal parameters that minimize the over-potential difference η and improve the efficiency using a newly developed bat swarm algorithm with a variable population embedded in the computational intelligence-aided design. The simulation results were in agreement with previously reported results, suggesting that the proposed technique has potential applications for automating and optimizing the design of PEFCs.

Introduction

As a result of the increasing need for an efficient and clean energy supply, considerable importance has been placed on the advancement and fundamental research of polymer electrolyte fuel cell (PEFC) technology. Among the components of PEFCs, the cathode plays a key role in the operation of PEFCs, in which an oxygen reduction reaction (ORR) occurs and generates heat. Platinum (Pt) loading, ionic conductivity, and the reaction's exchange current density are among the factors that may affect the performance. Numerous studies have been conducted to develop models and approaches that are essential to battery performance and optimization.

Springer et al. [1] presented an isothermal, one-dimensional, steady-state model for a PEFC with a Nafion 117 membrane, in which the water diffusion coefficients, electro-osmotic drag coefficients, water sorption isotherms, and membrane conductivities were employed. Bernardi and Verbrugge [2] developed a mathematical model of the solid-polymer-electrolyte fuel cell, and they utilized this model to investigate the factors that affect the performance of the fuel cell and to elucidate the mechanism for the transport of species in a complex network of gas, liquid and solid phases. Amphlett et al. [3] reported a parametric model for predicting the performance of a solid PEFC by considering the mass transport properties. Bevers et al. [4] presented a one-dimensional dynamic model of a gas diffusion electrode that considered the various effects of parameter changes. Kulikovsky [5] developed a two-dimensional model of the cathode compartment of a PEFC with gas channels. Rowe and Li [7] proposed a one-dimensional non-isothermal model of a PEFC to investigate the effects of various design and operating conditions on the cell performance. Baschuk and Li [6] formulated a mathematical model for the performance and operation of a single PEFC. Song et al. [8] utilized the AC impedance method to optimize the thickness and composition of the supporting PEFC layer. Ramadass et al. [9] developed a semi-empirical approach of capacity fade prediction for Li-ion cells, which considers the active material and rate capability losses. Wang et al. [10] investigated the effects of different operating parameters on the performance of PEFCs through an experiment that employed pure hydrogen on the anode side and air on the cathode side. Yerramalla et al. [11] developed a mathematical model to investigate the dynamic performance of a PEFC with a number of single cells combined into a fuel cell stack. Song et al. [12] investigated one- and two-parameter numerical optimization analyses of PEFC cathode catalyst layers that consider the Nafion content, Pt loading, catalyst layer thickness and porosity. Grujicic and Chittajallu [13] developed a model for determining the air-inlet pressure, cathode thickness and length, and the width of the shoulders in the inter-digitized air distributor. Weber and Newman [14] reviewed the models of PEFCs, the general modeling methodologies and some related summaries. Pathapati et al. [15] reported a mathematical model for simulating the transient phenomena in a PEFC that can predict the transient response of cell voltage, temperature, hydrogen/oxygen out flow rates and cathode and anode channel temperatures/pressures under sudden changes in load current. Tao et al. [16, 17] developed a three-dimensional, two-phase and non-isothermal model and carried out the parameter sensitivity analysis. Wang et al. [18] utilized a three-dimensional model to analyze the effect of the design parameters in a bipolar plates with the serpentine flow field. Wang and Feng [19–21] reported a one-dimensional study on electrochemical phenomena within the cathode. Wang et al. [22] reviewed recent PEFC technical progress and applications, the role of fundamental research in fuel-cell technology and the major challenges in fuel-cell commercialization. Khajeh-Hosseini-Dalasm et al. [23] proposed a computational study of the cathode catalyst layer of a PEFC and structural parameters analysis. Gao et al. [24] presented a multi-physical dynamic fuel cell stack model. Wang et al. [25, 26] investigated an inverse

geometry design problem for optimization of single serpentine and transient characteristics of PEFC with parallel and interdigitated flow fields using a three-dimensional, two-phase model. Jung et al. [27] developed an elaborate simulation model of the fuel cell stack system. Askarzadeh and Rezazadeh [28] proposed an innovative global harmony search algorithm for parameter identification of a SR-12 Modular polymer electrode membrane(PEM) Generator. Wang et al. [29] carried out the parameter sensitivity analysis for a three-dimensional, two-phase, non-isothermal model of polymer electrolyte membrane fuel cell. Chen et al. [30] proposed a quantitative approach for predicting the remaining battery life by using an adaptive, bathtub-shaped function. Considering thermoelectric and thermoeconomic objectives, Sayyaadi and Esmaeilzadeh [31] developed a methodology for optimal PEFC control, in which the net power density and energetic efficiency are maximized. Pathak and Basu [32] discussed a mathematical model for the anode and cathode with an anion-exchange membrane for predicting the performance of a fuel cell considering reaction kinetics and ohmic resistance effects. Noorkami et al. [33] investigated the temperature uncertainty as a key parameter in determining the performance and durability of a PEFC. Molaeimanesh and Akbari [34] proposed a three-dimensional lattice Boltzmann model of a PEFC cathode, in which the electrochemical reaction on the catalyst layer is able to simulate single- and multi-species reactive flow in a heterogeneous, anisotropic gas diffusion layer. Wang et al. [35] studied a three-dimensional, two-phase, and non-isothermal fuel cell model incorporating the Leverett-Udell correlation and evaluated its performance.

Although there have been a large number of previous studies, the available literature on the analytical modeling of cathode electrodes fails to address two concerns. First, the previous studies do not capture the coupling effects on PEFC performance resulting from the interactions among the design variables. Second, few effective methods have been developed that allow for quantitative analysis, model verification, and parameter optimization. To fill this void, this paper proposes a bat swarm algorithm with a variable population (BAVP) to construct and optimize the quantitative cathode electrode model, which will be embedded into the computational intelligence-aided design (CIAD) [36] framework. This new CIAD framework provides an expanded capability to accommodate a variety of CI algorithms, and it has three advantages: (1) mobilizing computational resources; (2) taking advantage of multiple CI algorithms; and (3) reducing computational costs. This framework has been demonstrated in some of our previous works in diverse areas: applied energy [30], new drug development for public healthcare [37, 38], economy and finance [39], sustainable development [40–42], aerospace engineering [43], automotive engineering [44], public security [45], and engineering modeling and design [46, 47], among others.

Inspired by the echolocation behavior of bats and first proposed by Yang [48] in 2010, the bat swarm algorithm (BA) allocates computational resources by adjusting its population and accelerating the calculation speed. By using echolocation, a swarming bat can quickly respond to changes in the direction and

speed of its neighbors during activities such as detecting prey, avoiding obstacles, and locating roosting crevices in dark surroundings. Useful behavioral information is passed among bats and guides them to move from one configuration to another as one unit. By borrowing this intelligence of social behavior, the BAVP is parallel, independent of initial values, and able to achieve a global optimum.

This work has three main contributions. First, our model can effectively assess PEFC performance. Second, a BAVP swarm intelligence method is devised as the search engine to optimize the model parameters embedded in the CIAD framework. Third, two new metrics, the index of moving mean of the average precision (mmAP) and the index of moving mean of variance (mmVAR), are introduced to characterize the dynamic evolutionary behaviors.

The remainder of this paper is organized as follow: Section 2 (Analytical Modeling) discusses the analytical modeling of the cathode electrode; Section 4 (Computational intelligence-aided design) describes the conceptual framework of CIAD and the integrated solver; Section 3 (Bat swarm algorithm with variable population) describes the BAVP algorithm for the optimization; Section 5 (Optimization and Parameter Determination) defines the fitness function for optimizing the analytical model using the model proposed in Section 2; Section 6 (Empirical Results and Discussion) presents the empirical results and further verifies the optimal design; and Section 7 (Conclusions and Future Works) concludes the paper.

Analytical Modeling

A schematic diagram of a dual-layer configuration of a cathode electrode is shown in Fig. 1, in which five specific areas are numbered and are explained below. The left side of the electrode attaches to the PEM, and the right side connects to the diffusion media [19, 20].

① Includes the assumption that the oxygen concentrations, temperatures, electronic phase potentials, and equilibrium potential are the same between the two layers and are uniform within each layer. The electrodes are thin layers ($\leq 10\mu$m) coated on the PEM surface containing a catalyst (typically **Pt**), carbon(**C**), an ionomer electrolyte and void space. In general, there are three phases in the electrode: (i) void space for the transport of gaseous reactants, (ii) ionomer content for the transfer of protons, and (iii) carbon support for conducting electrical current. In addition to the electrochemical catalyst, which is essential for all functions, equation (1) is given.

$$O_2 + 4e^- + 4H^+ \rightarrow 2H_2O + Heat \quad (1)$$

② The two sub-layers are denoted as 'Layer 1' and 'Layer 2'. Five parameters are considered in this model that include the ionic conductivity σ_m, the catalyst specific area a, the exchange current density i, the ionic resistance R_δ, the

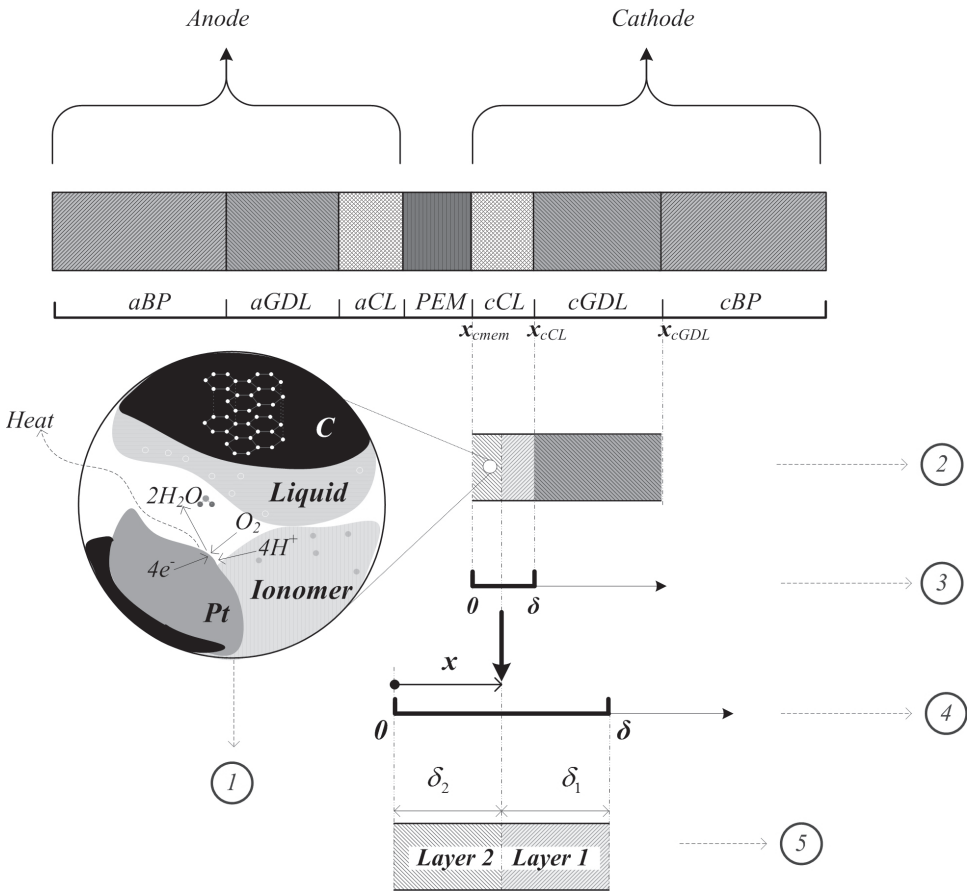

Fig. 1. Schematic of a dual-layer cathode electrode of a PEFC.

doi:10.1371/journal.pone.0114223.g001

current density I_δ, the thickness of sub-layer δ, the interface location of the two sub-layers l, and so on.

The ionic conductivity factors σ_m of 'Layer 1' and 'Layer 2' are σ_1 and σ_2, respectively, and they are determined from the electrolyte water content λ, the ionomer tortuosity τ_m, the Nafion content ϵ_m and the temperature T, as given in equation (2). The ratio of the ionic conductivity factors of 'Layer 1' and 'Layer 2' is given in equation (3).

$$\sigma_m = \epsilon_m^{\tau m}(0.5139\lambda - 0.326)\exp\left[1268\left(\frac{1}{303} - \frac{1}{T}\right)\right] \tag{2}$$

$$r_\sigma = \frac{\sigma_1}{\sigma_2} \tag{3}$$

The catalyst specific area a describes the active catalyst surface area per unit volume. The exchange current density i depends on factors such as temperature and the electrochemical characteristics of the catalyst. As shown in equation (4), the factor of the catalyst specific area and the exchange current density multiplication ai is determined by factors such as the structural feature of the electrode, including the reaction interface roughness and the mean radius of the catalyst particles, and is the most important factor for catalyst cost reduction, where E_a is the activation energy for the ORR; R_g is the universal gas constant, 8.314 J/mol K; and s is the liquid water saturation. The ratio of ai of 'Layer 1' and 'Layer 2' is given in equation (5).

$$ai = ai_0(1-s)\exp\left[-\frac{E_a}{R_g}\left(\frac{1}{T}-\frac{1}{353.15}\right)\right] \tag{4}$$

$$r_{ai} = \frac{ai_1}{ai_2} \tag{5}$$

③ A lumped variable ΔU is defined in equation (6), in which $R_\delta = \delta/\sigma_m$ is the overall ionic resistance across the cathode electrode, and $I_\delta = -j_\delta\delta$ is the current density based on the transfer current density j_δ at the interface between the two electrodes.

$$\Delta U = R_\delta I_\delta \tag{6}$$

④ The relative location of the interface between the two sub-layers is defined in equation (7), in which δ is the total thickness of the dual-layer electrodes.

$$l = \frac{x}{\delta} \tag{7}$$

⑤ The thickness ratio of the two sub-layers r_δ is defined in equation (8)

$$r_\delta = \frac{\delta_1}{\delta_2} \tag{8}$$

Considering the cathode electrode in one dimension (x direction), the two indices (η_1 and η_2) of the over-potential difference of 'Layer 1' and 'Layer 2' are given in equations (9) and (10), respectively, where Π, $\mathbf{\Psi}$ and Ω are defined in equations (11) to (13) [21].

$$\eta_1(\Delta U, l) = \frac{R_g T}{\alpha_c F}\ln[\Pi(\Delta U, l)+1] \tag{9}$$

$$\eta_2(\Delta U,r_\sigma,r_{ai},r_\delta,l)=\frac{R_gT}{\alpha_cF}\ln[\mathbf{\Psi}(\Delta U,r_\sigma,r_{ai},r_\delta)(\Omega(\Delta U,r_\sigma,r_{ai},r_\delta,l)+1)] \quad (10)$$

$$\Pi(\Delta U,l)=\tan^2\left(\pm\left(\Delta U\frac{\alpha_cF}{2R_gT}\right)^{\frac{1}{2}}\cdot(1-l)\right) \quad (11)$$

$$\mathbf{\Psi}(\Delta U,r_\sigma,r_{ai},r_\delta)=\Pi\left(\Delta U,\frac{1}{1+r_\delta}\right)(1-r_\sigma r_{ai})+1 \quad (12)$$

$$\Omega(\Delta U,r_\sigma,r_{ai},r_\delta,l)= \tan^2\left(\begin{array}{c}\sqrt{\Delta U\frac{\alpha_cF}{2R_gT}\cdot\frac{r_\sigma}{r_{ai}}\cdot\mathbf{\Psi}(\Delta U,r_\sigma,r_{ai},r_\delta)}\cdot\left(l-\frac{1}{1+r_\delta}\right)\\ -\tan^{-1}\sqrt{\frac{\Pi\left(\Delta U,\frac{1}{1+r_\delta}\right)}{\mathbf{\Psi}(\Delta U,r_\sigma,r_{ai},r_\delta)}r_\sigma r_{ai}}\end{array}\right) \quad (13)$$

Bat swarm algorithm with variable population

Because the BAVP is inspired by the echolocation characteristics of bat swarms, it can be idealized to include the four following assumptions:

- 1 As shown in Fig. 2, all artificial bats (ABs) utilize the same echolocation mechanism to measure distance, and each AB individual B_i is able to detect the difference between prey (food) and obstacles.
- 2 Each individual B_i can generate ultrasounds to echolocate the prey and obstacles with a velocity of $v_{i,j}$ and a position of $x_{i,j}$ at time j, which are stated in Equations (15) and (14), respectively, where x_* is the current global best position.

$$x_{i,j+1}=v_{i,j}+x_{i,j} \quad (14)$$

$$v_{i,j+1}=v_{i,j}+(x_{i,j}-x_*)f_{i,j} \quad (15)$$

- 3 Each individual B_i can adjust the frequency of the ultrasounds $f_{i,j}$ at time j within a range of $[f_{min}, f_{max}]$, corresponding to a wavelength λ in the range of $[\lambda_{min}, \lambda_{max}]$ and a loudness A in the range of $[A_{min}, A_{max}]$, as given in Equation (16), where β is a random vector of uniform distribution in the range of [0,1].

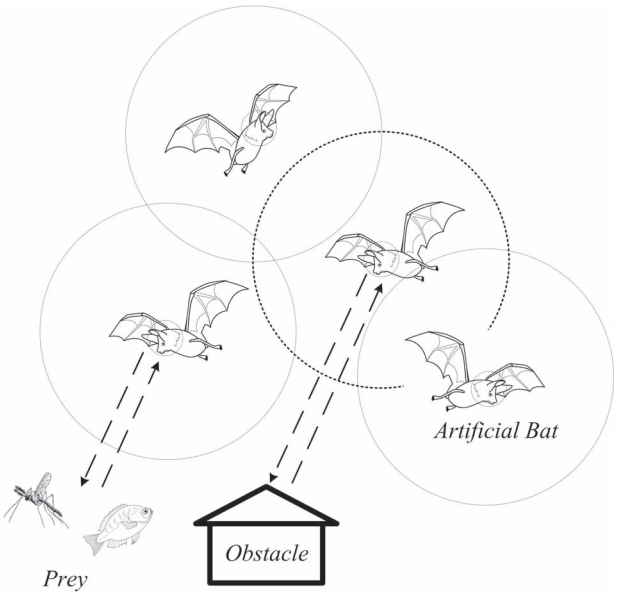

Fig. 2. The behaviors of bat swarms.

doi:10.1371/journal.pone.0114223.g002

$$f_{i,j} = f_{min} + (f_{max} - f_{min})\beta \tag{16}$$

- 4 As shown in Equation (17), the population P_j of ABs varies from time j to another, which accelerates the optimization process, in which P_N is the non-replaceable population and P_{R_j} is the replaceable population at time j.

$$P_j = P_N + P_{R_j} \tag{17}$$

As shown in Fig. 3, the following six steps are included in the BAVP flow chart: step (1), initialization; step (2), fitness evaluation; step (3), global solution generation; step (4), local solution generation; step (5), update solutions by using the global and local solutions; and step (6), check termination condition of convergence.

- Step (1), start program and initialize parameters and solutions; all artificial bats are moving randomly.
- Step (2), evaluate fitness for each solution.
- Step (3), generate new global solutions x, update velocities and adjust frequencies using equations (14) to (16).
- Step (4), generate new local solutions x^0 using Equation (18), where $\epsilon \in [-1,1]$ is a random-walk factor. As defined in Equation (19), $A_{i,j}$ is the loudness of the bat B_i at time j, in which $\alpha \in [0,1]$ is a reduction factor.

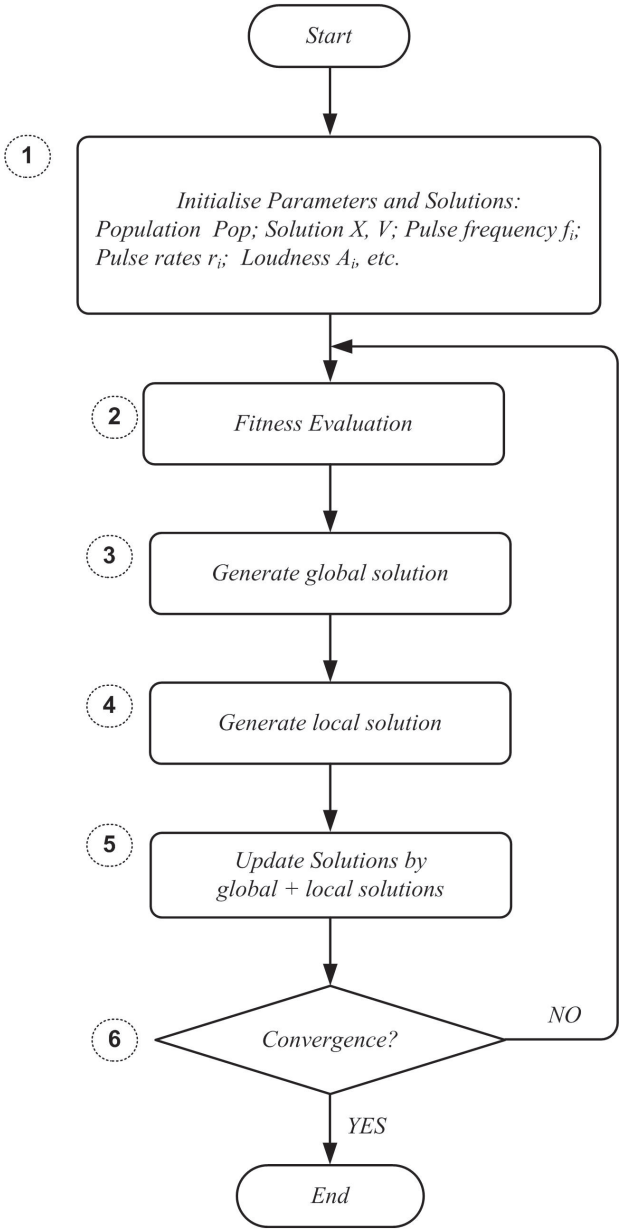

Fig. 3. BAVP flowchar.

doi:10.1371/journal.pone.0114223.g003

$$x^0_{i,j+1} = x^0_{i,j} + \epsilon A_{i,j} \tag{18}$$

$$A_{i,j+1} = \alpha A_{i,j} \tag{19}$$

- Step (5), compare the local and global solutions and update solutions, as given in Equation (20).

$$x_{i,j} = \begin{cases} x_{i,j} & \left(\text{if } x_{i,j} \geq x_{i,j}^0\right) \\ x_{i,j}^0 & \left(\text{otherwise } x_{i,j} < x_{i,j}^0\right) \end{cases} \tag{20}$$

- Step (6), continue running the calculation until the terminal conditions have been satisfied.

Computational intelligence-aided design

Computational intelligence (CI) is a set of nature-inspired approaches that provides numerous capabilities for solving complex problems. Compared to the traditional optimization methods, CI does not need to reformulate the problem to search a non-linear or non-differentiable space. Another advantage of CI is its flexibility in formulating the fitness function, which can be expressed as a function of the system output. This feature is particularly appealing if an explicit objective function is difficult to obtain.

Fig. 4 illustrates the CIAD framework, and the entire optimization process can be summarized in the following three main steps:

- *Step 1*, pre-process. In this step, quantitative models under specific conditions are obtained for engineering applications.
- *Step 2*, optimal design. This step defines the fitness functions according to the design objectives.
- *Step 3*, post-process. This step produces the final results and completes the post-processing tasks. Specifically, this step reports the optimal solution, analyses and visualizes the results, and presents the recommendations to policy makers. The 'CI integrated solver'(CIS) is employed to optimize the parameters for the fitness function, and the details of the CIS are given in Fig. 5.

As shown in Fig. 5, the conceptual framework of CIS consists of three parts: data input, the CI integrated solver and result output, as follows.

Part 1: Data Input (@point A). This part prepares the data input for the CI integrated solver. It collects, filters, stores, and pre-processes data originating from various sources, such as statistical yearbooks, research analyses, and government reports.

Part 2: CI Integrated Solver. In this part, a set of nature-inspired computational approaches are integrated into one solver to optimize complex real-world problems, which primarily involves one or more of the following methods: artificial neural networks, a genetic algorithm, fuzzy logic, simulated annealing, artificial immune algorithms, and swarm intelligence algorithms. In this paper, a BAVP algorithm (@point C) is

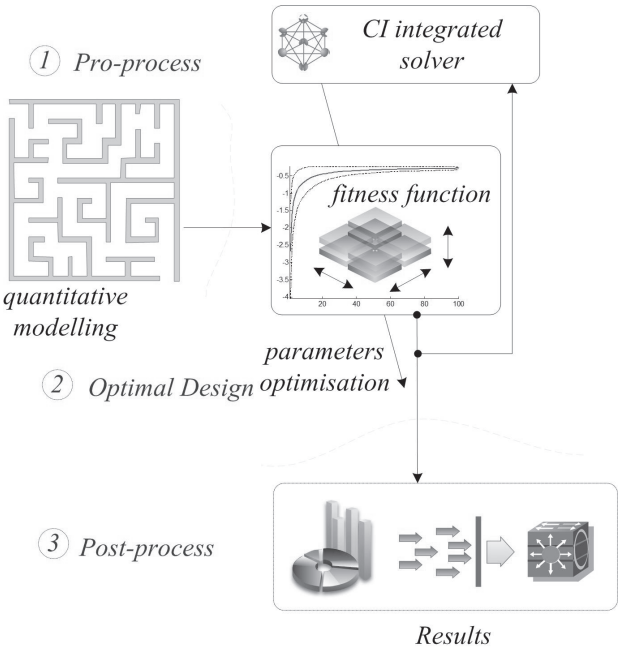

Fig. 4. Framework of computational intelligence-aided design.

doi:10.1371/journal.pone.0114223.g004

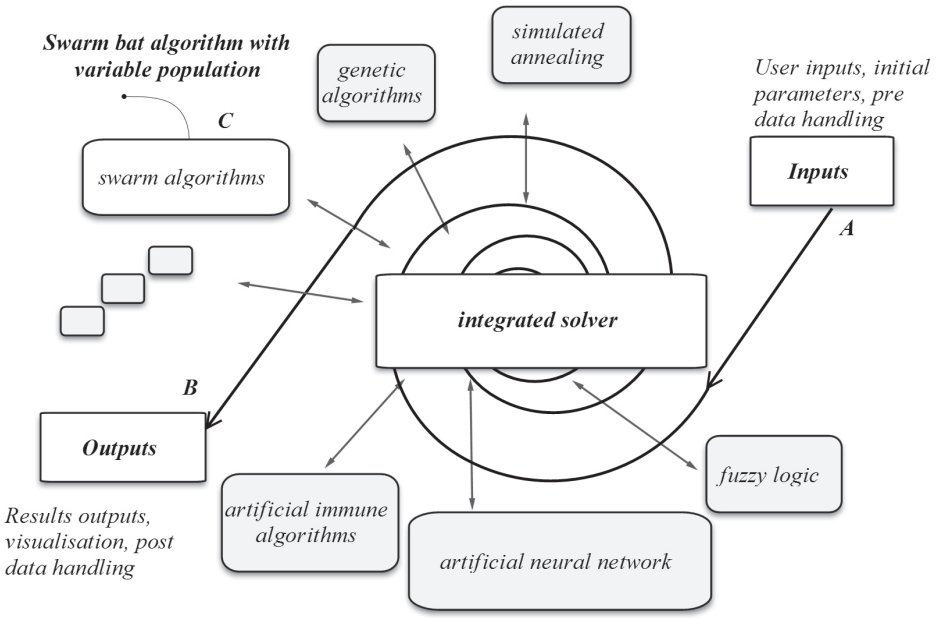

Fig. 5. The conceptual framework of the computational intelligence integrated solver.

doi:10.1371/journal.pone.0114223.g005

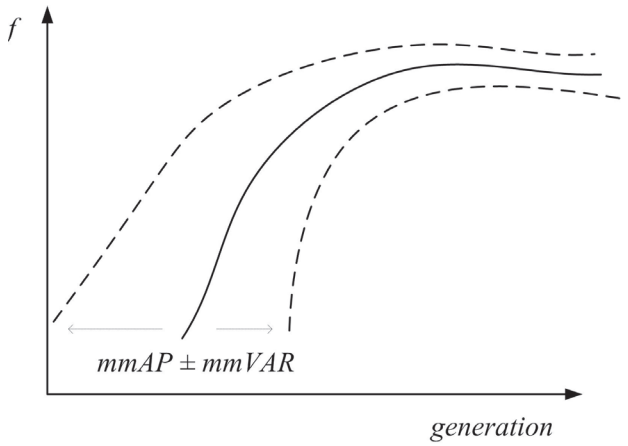

Fig. 6. The diagram of mmAP ± mmVAR over the full generations.

doi:10.1371/journal.pone.0114223.g006

embedded in this solver, and the details of this algorithm are discussed in Section 3.

Part 3: Result Output (@point B). This part reports the final results from Part 2. As shown in Fig. 4, the data-flow from Steps 4 to 3 is the input of the 'CI integrated solver' interconnected with point A, and the data-flow from Steps 3 to 2 is the output of the 'CI integrated solver' interconnected with point B.

Optimization and Parameter Determination

To determine the optimal parameters for the over-potential difference η, this section introduces two trend indices *mmAP* and *mmVAR* for evolutionary optimization, which are given in equations (21) and (22), respectively.

As stated in Equation (21), the index of *mmAP* is a moving average score of the mean value of vector f_j, where $i = 1,2,\cdots,p$, p is the population of the data set, and $MEAN(\cdot)$ is the average function. The index of *mmVAR* is a moving average score of the VAR value of vector f_j, as given in Equation (22), where $VAR(\cdot)$ is the variance function. The two indices are employed to assess the short-term fluctuations by capturing the longer-term trend across the evolutionary process.

$$mmAP(f_j) = \frac{1}{p}\sum_{i=1}^{p}\left(\frac{1}{i}\sum_{j=1}^{i} MEAN(f_j)\right) \tag{21}$$

$$mmVAR(f_j) = \frac{1}{p}\sum_{i=1}^{p}\left(\frac{1}{i}\sum_{j=1}^{i} VAR(f_j)\right) \tag{22}$$

Table 1. Parameters of the Swarmbat optimization.

max generations		100
test number		100
frequency range		[20000,500000]Hz
reduction factor	α	0.9
population		50
random step		0.01
lumped variable	ΔU	[0,0.1]V
ratio of ionic conductivity	r_σ	[0,2]
ratio of ai	r_{ai}	[0,2]
ratio of thickness	r_δ	[0,4]
location factor	l	[0,1]

doi:10.1371/journal.pone.0114223.t001

In Fig. 6, the solid line represents the *mmAP* scores for each vector f_j as given in Equation (21). The dashed lines are the $mmAP \pm mmVAR$ for each vector f_j as given in equation (22), which defines the limits of evolutionary paths of the optimization process (generation versus fitness f) as the upper and lower boundaries.

The fitness function F is in a reciprocal form of the over-potential difference function, as given in Equation (23). The fitness function is defined as the *mmAP* reciprocal function of the over-potential difference function η, in which maximizing F is a way to minimize η, and the goal of this function is to determine the optimal combination of five parameters, ΔU, r_σ, r_{ai}, r_δ and l, that simultaneously minimizes the objective of η. *eps* is the floating-point relative accuracy, which prevents singularity in the case where η is approaching 0 and F is approaching ∞.

$$F(\Delta U, r_\sigma, r_{ai}, r_\delta, l) = maximize : \left\{ mmAP\left(\frac{1}{\eta + eps}\right)\right\} \tag{23}$$

The over-potential difference function η is given in Equation (24), where ΔU is the lumped variable, given in Equation (6); r_σ is the ratio of the ionic conductivity of the two sub-layers, given in Equation (3); r_{ai} is the ratio of *ai*, given in Equation

Table 2. Optimal results of 'MEAN $\pm$ VAR'.

Parameters	Results
ΔU	0.07754 $\pm$ 0.01034 V
r_σ	1.03191 $\pm$ 0.12681
r_{ai}	0.85241 $\pm$ 0.13736
r_δ	2.05281 $\pm$ 0.16181
l	0.40709 $\pm$ 0.15818

doi:10.1371/journal.pone.0114223.t002

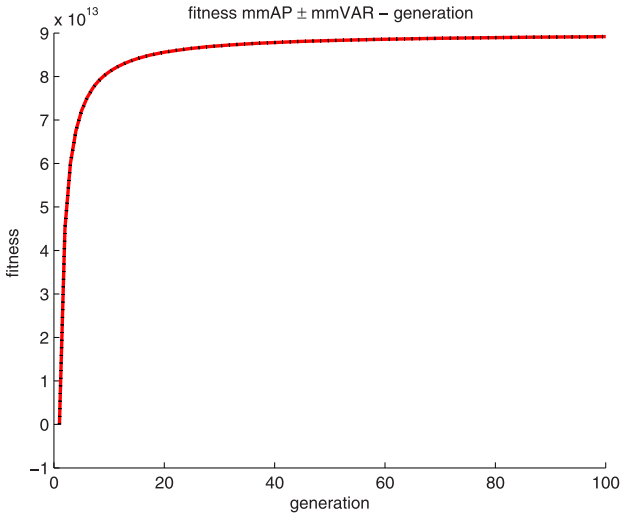

Fig. 7. Fitness curves of mmAP ± mmVAR over the simulation.

doi:10.1371/journal.pone.0114223.g007

(5); r_δ is the ratio of the thickness, given in Equation (8); and l is the location factor, given in Equation (7).

$$\eta(\Delta U, r_\sigma, r_{ai}, r_\delta, l) = \eta_1 \cdot \left(\frac{1}{1+r_\delta} \le l \le 1 \right) + \eta_2 \cdot \left(0 \le l \le \frac{1}{1+r_\delta} \right) \tag{24}$$

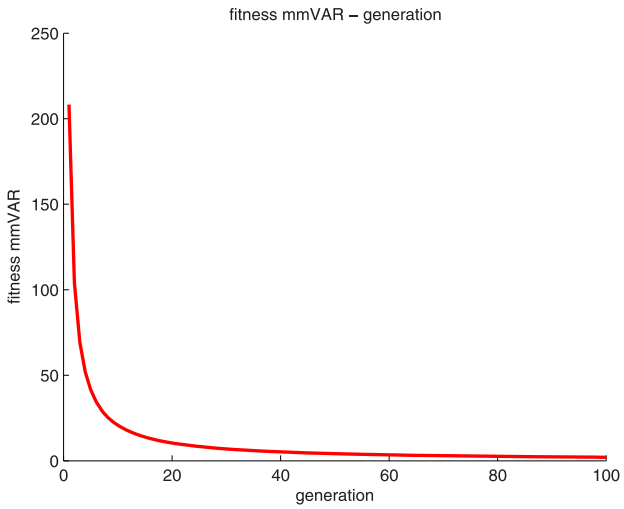

Fig. 8. Fitness curves of mmVAR over the simulation.

doi:10.1371/journal.pone.0114223.g008

Table 3. Impacts of five coupled variables on η in 3D figures.

Figure No.	$X-Y-Z$ axis
Figure 9	$\Delta U-r_{\sigma}-\eta$
Figure 10	$\Delta U-r_{ai}-\eta$
Figure 11	$\Delta U-r_{\delta}-\eta$
Figure 12	$\Delta U-l-\eta$
Figure 13	$r_{\delta}-l-\eta$
Figure 14	$r_{\sigma}-l-\eta$
Figure 15	$r_{ai}-l-\eta$

doi:10.1371/journal.pone.0114223.t003

Empirical Results and Discussion

Maximizing the fitness function F yields the minimum of η, which is performed using the specially designed toolboxes *SwarmBat* [49] and *SECFLAB* [50]. The computer specifications for the simulations are a 2.1 GHz Intel dual-core processor, Windows XP Professional v5.01 Build 2600 service pack 3, a 2.0 GB 800 MHz dual channel DDR2 SDRAM, and MATLAB R2008a.

The initial parameters are listed in Table 1, in which the max-generation number is 100, and it serves as the termination condition in each test. The test number is also 100. The frequency range is set to $[20000,500000]Hz$. The reduction factor α is 0.9. The population is 50, in which the non-replaceable P_N and replaceable population P_R are 40 and 10, respectively. The random step is 0.01, and the ranges of ΔU, r_{σ}, r_{ai}, r_{δ}, and l are [0,10], [0,10], [0,10], [0,2] and [0,3], respectively.

Table 2 presents the optimal combinations (MEAN$\pm$VAR) of ΔU, r_{σ}, r_{ai}, r_{δ} and l, which indicates that the over-potential is non-uniform within the cathode

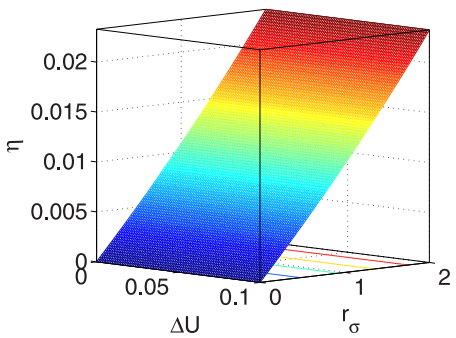

Fig. 9. η **vs.** ΔU **and** r_{σ}.

doi:10.1371/journal.pone.0114223.g009

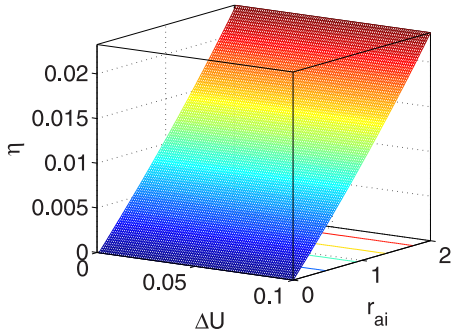

Fig. 10. η **vs.** ΔU **and** r_{ai}.

doi:10.1371/journal.pone.0114223.g010

and at particularly high values of the lumped parameter ΔU and is sensitive to the spatial variation l.

Fig. 7 shows the *mmAP* curves with the upper and lower *mmVAR* boundaries, in which the *mmVAR* boundaries stick to the *mmAP* fitness curves and the fitness increases very quickly; it reaches a plateau from generations 1 to 60 (or so), and it remains steady from generation 60 to 100. Note that all lines converge in generation 100.

Fig. 8 shows the fitness *mmVAR* over the entire simulation. The curves decline quickly within approximately 60 generations and finally reach 0 in generation 100. Figs. 7 and 8 indicate that the proposed optimization algorithm is efficient and accurate.

As also listed in Table 3, to demonstrate the impacts of the five coupled variables on η, Figs. 9 and 15 provide seven '3D' figures to evaluate these impacts.

Specifically, Figs. 9 and 10 show that r_σ and r_{ai} have similar positive effects on η, indicating that when r_σ and r_{ai} increase, η increases, and vice versa. Furthermore, when r_σ and r_{ai} remain constant, ΔU has limited effects on η.

Fig. 11 shows that η is sensitive to $r_\delta \in [3,4]$ and $\Delta U < 0.05$. Fig. 12 indicates that η increases faster with $l > 0.5$ and $\Delta U < 0.05$ and that better η values are obtained with larger l and smaller ΔU.

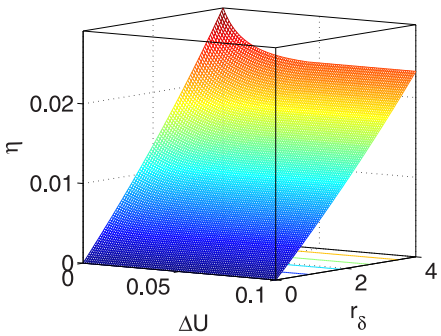

Fig. 11. η **vs.** ΔU **and** r_δ.

doi:10.1371/journal.pone.0114223.g011

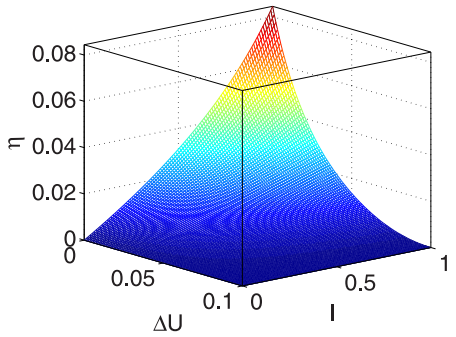

Fig. 12. η **vs.** ΔU **and** l.

doi:10.1371/journal.pone.0114223.g012

Fig. 13 shows that η is sensitive to smaller r_δ or ΔU. In Fig. 14, there is a plateau within $r_\sigma < 1$ and $l < 0.5$; furthermore, η is sensitive to larger l when $r_\sigma < 1$. When $r_\sigma \pm > 1$ and increases, η decreases within the full l range.

Fig. 15 shows that η increases when both r_{ai} and l become smaller, which implies that η is unstable with small values of r_{ai} and l.

Conclusions and Future Works

In this study, an analytical model that incorporates five parameters is proposed to explore the transport and electrochemical phenomena in dual-layered cathode electrodes of polymer electrolyte fuel cells. These parameters include the lumped variable ΔU, the ratio of the ionic conductivity of two sub-layers r_σ, the *ai* ratio of the two sub-layers r_{ai}, the ratio of the thickness r_δ and the relative location factor l. Moreover, a theoretical study on the spatial distribution of reaction rates across the electrode is presented.

The proposed model is utilized to define a design objective: determining the optimal combinations of the five parameters to minimize the over-potential difference η. Based on the trend indices mmAP and mmVAR, a fitness function

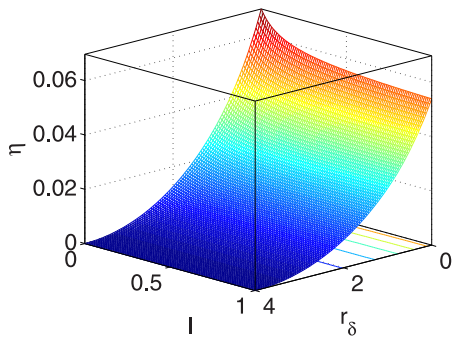

Fig. 13. η **vs.** r_δ **and** l.

doi:10.1371/journal.pone.0114223.g013

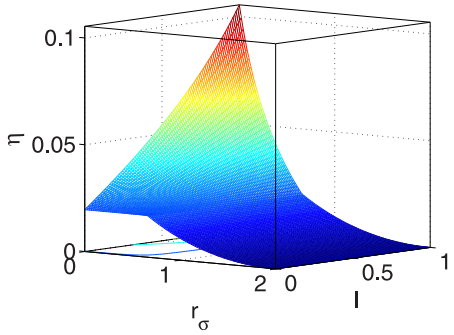

Fig. 14. η **vs.** r_σ **and** l.

doi:10.1371/journal.pone.0114223.g014

was constructed with the five variables as discussed above, which are optimized by the bat swarm algorithm with a variable population.

The numerical solutions obtained in this study were applied to optimize the electrode performance through a set of optimal dual-layer configurations, and the research findings are summarized in the following three points:

1. The proposed dual-layered cathode electrode model for the determination of the optimal parameters provides a strong argument for implementing the solutions to explore the impacts of each layer's properties on their performance.
2. Based on the developed dual-layered cathode electrode model, a bat swarm algorithm with a variable population is developed, which directly affects the determination of the optimal parameters due to its high efficiency and accuracy.
3. The proposed two trend indices *mmAP* and *mmVAR* were utilized to smooth out short-term fluctuations and highlight longer-term trends until the maximum generation fitness point was reached, which helps to measure the computational performance of the BAVP or to deploy other algorithms.

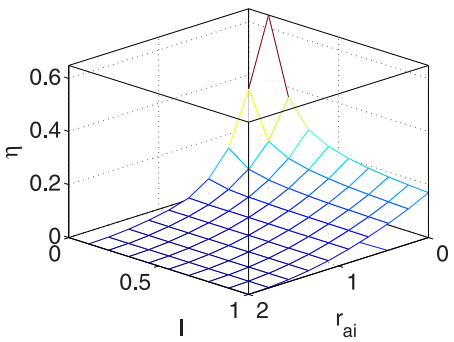

Fig. 15. η **vs.** r_{ai} **and** l.

doi:10.1371/journal.pone.0114223.g015

Our future research will focus on developing new types of CI algorithms, such as the swarm dolphin algorithm [51], the swarm wolf algorithm and their hybrid derivatives, to optimize further geometrical parameters and optimal combinations for improving the efficiency of polymer electrolyte fuel cells with multiple-layer configurations. To achieve a 'state-of-practice' design framework for the fuel cell, further experimental research is needed to establish an advanced model for chemical-dynamical coupled behavior and the potentials of fuel cell commercialization.

Acknowledgments

The authors would like to acknowledge the partial support provided by the National Natural Science Foundation of China (No. 91123023 and 51105061) and by the National Program for Support of Top-Notch Young Professionals. We would like to express our appreciation to Prof. Yun Wang for his useful discussions and suggestions.

Furthermore, the authors would like to acknowledge the two anonymous reviewers and the academic editor for their valuable comments on this paper.

Author Contributions

Conceived and designed the experiments: YC WNH BP. Performed the experiments: YC WNH BP. Analyzed the data: YC WNH BP. Contributed reagents/materials/analysis tools: YC WNH BP. Wrote the paper: YC BP. Conceived initial ideas of this manuscript: YC BP. Designed the software used in analysis: YC. Simulations: YC WNH.

References

1. **Springer TE, Zawodzinski TA, Gottesfeld S** (1991) Polymer electrolyte fuel cell model. J Electrochem Soc 138: 2334–2342.
2. **Bernardi DM, Verbrugge MW** (1992) A mathematical model of the solid-polymer-electrolyte fuel cell. J Electrochem Soc 139: 2477–2491.
3. **Amphlett JC, Baumert RM, Mann RF, Peppley BA, Roberge PR, et al.** (1995) Performance modeling of the ballard mark iv solid polymer electrolyte fuel cell. J Electrochem Soc 142: 1–8.
4. **Bevers D, Wohr M, Yasuda K, Oguro K** (1997) Simulation of a polymer electrolyte fuel cell electrode, J Appl Electrochem 27: 1254–1264.
5. **Kulikovsky AA, Divisek J, Kornyshev AA** (1999) Modeling the cathode compartment of polymer electrolyte fuel cells: dead and active reaction zones. J Electrochem Soc 146: 3981–3991.
6. **Baschuk JJ, Li XG** (2000) Modelling of polymer electrolyte membrane fuel cells with variable degrees of water flooding. J Power Sources 86: 181–196.
7. **Rowe A, Li XG** (2001) Mathematical modeling of proton exchange membrane fuel cells. J Power Sources 102: 82–96.
8. **Song JM, Cha SY, Lee WM** (2001) Optimal composition of polymer electrolyte fuel cell electrodes determined by the AC impedance method. J Power Sources 94: 78–84.

9. **Ramadass P, Haran B, White R, Popov BN** (2003) Mathematical modeling of the capacity fade of Li-ion cells. J Power Sources 123: 230–240.
10. **Wang L, Husar A, Zhou TH, Liu HT** (2003) A parametric study of PEM fuel cell performances. Int J Hydrogen Energ 28: 1263–1272.
11. **Yerramalla S, Davari A, Feliachi A, Biswas T** (2003) Modeling and simulation of the dynamic behavior of a polymer electrolyte membrane fuel cell. J Power Sources 124: 104–113.
12. **Song DT, Wang QP, Liu ZS, Navessin T, Eikerling M, et al.** (2004) Numerical optimization study of the catalyst layer of PEM fuel cell cathode. J Power Sources 126: 104–111.
13. **Grujicic M, Chittajallu KM** (2004) Design and optimization of polymer electrolyte membrane (PEM) fuel cells. Appl Surf Sci 227: 56–72.
14. **Weber AZ, Newman J** (2004) Modeling transport in polymer-electrolyte fuel cell. Chem Rev 104: 4679–4726.
15. **Pathapati PR, Xue X, Tang J** (2004) A new dynamic model for predicting transient phenomena in a PEM fuel cell system. Renew Energ 30: 1–22.
16. **Tao WQ, Min CH, Liu XL, He YL, Yin BH, et al.** (2006) Parameter sensitivity examination and discussion of PEM fuel cell simulation model validation: Part I. Current status of modeling research and model development. J Power Sources 160: 359–373.
17. **Min CH, He YL, Liu XL, Yin BH, Jiang W, et al.** (2006) Parameter sensitivity examination and discussion of PEM fuel cell simulation model validation: Part II: Results of sensitivity analysis and validation of the model. J Power Sources 160: 374–385.
18. **Wang XD, Duan YY, Yan WM, Peng XF** (2008) Local transport phenomena and cell performance of PEM fuel cells with various serpentine flow field designs. J Power Sources 175: 397–407.
19. **Wang Y, Feng XH** (2008) Analysis of reaction rates in the cathode electrode of polymer electrolyte fuel cell i. single-layer electrodes. J Electrochem Soc 155: A8–A16.
20. **Wang Y, Feng XH** (2009) Analysis of reaction rates in the cathode electrode of polymer electrolyte fuel cell ii. dual-layer electrodes. J Electrochem Soc 156: B403–B409.
21. **Feng XH, Wang Y** (2010) Multi-layer configuration for the cathode electrode of polymer electrolyte fuel cell. Electrochim Acta 55: 4579–4586.
22. **Wang Y, Chen KS, Mishler J, Cho SC, Adroher XC** (2011) A review of polymer electrolyte membrane fuel cells: Technology, applications, and needs on fundamental research. Appl Energy 88: 981–1007.
23. **Khajeh-Hosseini-Dalasm N, Kermani MJ, Ghadiri Moghaddama D, Stockie JM** (2010) A parametric study of cathode catalyst layer structural parameters on the performance of a PEM fuel cell. Int J Hydrogen Energ 35: 2417–2427.
24. **Gao F, Blunier B, Miraoui A, El-Moudni A** (2010) Proton exchange membrane fuel cell multi-physical dynamics and stack spatial non-homogeneity analyses. J Power Sources 195: 7609–7626.
25. **Wang XD, Huang YX, Cheng CH, Jang JY, Lee DJ, et al.** (2010) An inverse geometry design problem for optimization of single serpentine flow field of PEM fuel cell. Int J Hydrogen Energ 35: 4247–4257.
26. **Wang XD, Xu JL, Yan WM, Lee DJ, Su A** (2011) Transient response of PEM fuel cells with parallel and interdigitated flow field designs. Int J Heat Mass Tran 54: 2375–2386.
27. **Jung JH, Ahmed S, Enjeti P** (2011) PEM fuel cell stack model development for real-time simulation applications. IEEE Trans Ind Electron 58: 4217–4231.
28. **Askarzadeh A, Rezazadeh A** (2012) An innovative global harmony search algorithm for parameter identification of a pem fuel cell model. IEEE Trans Ind Electron 59: 3473–3480.
29. **Wang XD, Xu JL, Lee DJ** (2012) Parameter sensitivity examination for a complete three-dimensional, two-phase, non-isothermal model of polymer electrolyte membrane fuel cell. Int J Hydrogen Energ 37: 15766–15777.
30. **Chen Y, Miao Q, Zheng B, Wu SM, Pecht M** (2013) Quantitative analysis of lithium-ion battery capacity prediction via adaptive bathtub-shaped function (2013) Energies 6: 3082–3096.
31. **Sayyaadi H, Esmaeilzadeh H** (2013) Determination of optimal operating conditions for a polymer electrolyte membrane fuel cell stack: optimal operating condition based on multiple criteria. Int J Energ Res 37: 1872–1888.

32. **Pathak R, Basu S** (2013) Mathematical modeling and experimental verification of direct glucose anion exchange membrane fuel cell. Electrochim Acta 113: 42–53.

33. **Noorkami M, Robinson JB, Meyer Q, Obeisun OA, Fraga ES, et al.** (2014) Effect of temperature uncertainty on polymer electrolyte fuel cell performance. Int J Hydrogen Energ 39: 1439–1448.

34. **Molaeimanesh GR, Akbari MH** (2014) A three-dimensional pore-scale model of the cathode electrode in polymer-electrolyte membrane fuel cell by lattice Boltzmann method. J Power Sources 258: 89–97.

35. **Wang XD, Wang YL, Chen Y, Si C, Su A, et al.** (2014) Proton exchange membrane fuel cell modeling with diffusion layer-based and sands-based capillary pressure correlations: Comparative study. J Taiwan Inst Chem E 45: 1532–1541.

36. **Chen Y, Zhang GF, Jin TD, Wu SM, Peng B** (2014) Quantitative modelling of electricity consumption using computational intelligence aided design. J Clean Prod 69: 143–152.

37. **Xu YJ, Shi XF, Yang XW, Liu XH, Chen Y, et al.** (2012) Optimisation of extraction technology of schisandrae chinensis fructus by multi-objective genetic algorithm. Chin Pharm J 47: 669–673.

38. **Liu XH, Bai YE, Chen Y, Yang XW, Xu YJ, et al.** (2012) Non-dominated sorting genetic algorithm for multi-objective optimisation of aquous extraction conditions of floes trollii. Chin J Health Statis 29: 846–848.

39. **Chen Y, Zhang GF** (2013) Exchange rates determination based on genetic algorithms using mendel's principles: investigation and estimation under uncertainty. Inform Fusion 14: 327–333.

40. **Chen Y, Zhang GF, Li YY, Ding Y, Zheng B, et al.** (2013) Quantitative analysis of dynamic behaviours of rural areas at provincial level using public data of gross domestic product. Entropy 15: 10–31.

41. **Chen Y, Wang XY, Sha ZJ, Wu SM** (2012) Uncertainty analysis for multi-state weighted behaviours of rural area with carbon dioxide emission estimation. Appl Soft Comput 12: 2631–2637.

42. **Chen Y, Song ZJ** (2012) Spatial analysis for functional region of suburban-rural area using micro genetic algorithm with variable population size. Expert Syst Appl 39: 6469–6475.

43. **Chen Y, Cartmell MP** (2007) Multi-objective optimisation on motorised momentum exchange tether for payload orbital transfer. In: Proceedings of 2007 IEEE Congress on Evolutionary Computation (CEC). pp. 987–993.

44. **Chen Y, Wang ZL, Qiu J, Huang HZ** (2012) Hybrid fuzzy skyhook surface control using multi-objective micro-genetic algorithm for semi-active vehicle suspension system ride comfort stability analysis. J Dyn Syst-t ASME 134: 041003(14 pages).

45. **Chen Y, Ma Y, Lu Z, Peng B, Chen Q** (2011) Quantitative analysis of terahertz spectra for illicit drugs using adaptive-range micro-genetic algorithm. J Appl Phys 110: 044902–10.

46. **Chen Y, Wang ZL, Liu Y, Zuo MJ, Huang HZ** (2012) Parameters determination for adaptive bathtub-shaped curve using artificial fish swarm algorithm. In: 2012 Proceedings of The 58th Annual Reliability and Maintainability Symposium (RAMS).

47. **Chen Y, Peng B, Hao XH, Xie GN** (2014) Fast approach of pareto-optimal solution recommendation to multi-objective optimal design of serpentine-channel heat sink. Appl Therm Eng 70: 263–273.

48. **Yang XS** (2010) A new metaheuristic bat-inspired algorithm. In: J.R. Gonzlez, et al. (Eds.). Nature Inspired Cooperative Strategies for Optimization (NICSO 2010). Studies in Computational Intelligence 284, pp. 65–74.

49. **Chen Y** (2013) SwarmBat - The Artificial Bat Algorithm (ABA). Available: http://www.mathworks.cn/matlabcentral/fileexchange/39116-swarmbat-the-artificial-bat-algorithm-aba. Accessed 10 October 2014.

50. **Chen Y** (2013) SECFLAB - Simple Econometrics And Computational Finance Laboratory Toolbox. Available: http://www.mathworks.com/matlabcentral/fileexchange/38120. Accessed 10 October 2014.

51. **Chen Y** (2014) SwarmDolphin - The Swarm Dolphin Algorithm (SDA). Available: http://www.mathworks.com/matlabcentral/fileexchange/45965. Accessed 10 October 2014.